Final Report:

Using Surface Pressure to Improve Tropical Cyclone / Surface Wind Retrievals From SAR

PI Ralph Foster
Applied Physics laboratory
University of Washington
1013 NE 40th St
Seattle, WA, 98105-6698
phone: (206) 685-5201 fax: (206) 543-6785 email: ralph@apl.washington.edu

Co-I Jerome Patoux
Department of Atmospheric Sciences
University of Washington
Box 351640, Seattle, WA, 9895-1640

Award Number: N00014-08-1-1165

LONG-TERM GOALS

The calibration and validation of surface wind and stress retrievals from oceanic synthetic aperture radar (SAR) imagery is especially difficult in tropical cyclone (TC) conditions. The geophysical model functions (GMFs) that characterize the radar backscatter in terms of the near-surface wind vector for different viewing geometries are currently poorly characterized for the very high wind and strong ocean surface wave conditions that are present in all TCs. Our long-term goal is to develop a novel methodology to use surface pressure observations and a planetary boundary (PBL) model for calibration and validation (Cal/Val) of SAR GMFs in TC conditions and to produce scene-wide wind vector retrievals that are most consistent with the image backscatter, the GMF and the PBL model.

OBJECTIVES

The objectives of this research are to (1) develop the methodology for deriving TC SLP fields from first-guess surface wind vector estimates based on various GMF formulations; (2) Use these SLP fields to derive surface wind vector retrievals that are, in a least-squares sense, a scene-wide optimal surface wind retrieval that is consistent with the observable linear features in the SAR image, the GMF and the PBL model; (3) Develop an optimization scheme that seeks the minimum adjustment to the surface wind vector field that will minimize the difference between observed (e.g. via drop sondes or buoys) and SAR-derived bulk pressure gradients across the image. The optimized surface wind field can then be used either to assess or adjust the GMF.

APPROACH

GMFs describe the average radar backscatter from the sea surface in terms of the surface wind speed and the viewing geometry (incidence and azimuth angles). Scatterometers obtain multiple approximately simultaneous looks at multiple different viewing geometries (at least fore and aft looks) at the same patch of the sea surface. The incidence angles are known, so it is possible to estimate the most likely wind speed and azimuth angle (i.e. wind direction) that best explains to the separately measured radar backscatters from the different viewing geometries.

As compared to scatterometer wind vector retrievals, the standard method for obtaining surface wind vectors from SAR imagery is very difficult. The same GMFs are used, but there is only a single viewing geometry for each wind vector cell. Wind directions are estimated by identifying linear features in the imagery at scales ranging from ~0.5 km to 2-4 km wavelengths. These linear features are assumed to be the surface imprint of PBL coherent structures that roughly align with the surface wind (Foster, 1997; 2005; Morrison et al., 2005; Lorsolo et al. 2008; Zhang et al. 2008; Ellis and Businger, 2010). These linear features cannot be identified throughout the entire SAR scene (which is commonly about 450 by 450 km), so wind directions are interpolated between the identified linear features using different methods. These directions and the backscatter are input to the GMF and wind speeds are retrieved.

Our research is performed in collaboration with Chris Wackerman of General Dynamics (GD) and Jochen Horstmann of NATO Undersea Research Centre (NURC). GD and NURC have developed separate methods for estimating wind directions. The GD and NURC wind directions have been merged into a single wind direction product and incorporated into a new processing system (WiSAR) that produces surface wind vector maps at 1 km spacing. WiSAR has been installed and is being run by Mike Caruso at the Center for Southeastern Tropical Advanced Remote Sensing (CSTARS, Hans Graber director). We use the WiSAR wind vector fields as input to our SLP pattern and SLP-filtered surface wind retrieval system.

Because the pressure gradient force is a dominant term in the PBL momentum budget, the imprint of the surface stress field can be used to estimate the surface pressure gradient field through the use of a diagnostic PBL model. In its simplest form, PBL model assumes that the mean advective forces are relatively small and that the flow is neutrally-stratified and barotropic. Adding complexity, the PBL model includes the effects of thermal winds, boundary layer stratification, a gradient wind correction for curved flow and momentum entrainment across the boundary layer top. We significantly improved the nonlinear dynamics representation in terms of a modified gradient wind correction for TC conditions, which added a second tuning parameter to the PBL model. We also developed and included an important correction for the inherent radial dependence of boundary layer depth in a strong swirling vortex consistent with the vortex boundary layer model that was developed in Foster (2009).

Once the pressure gradient fields have been obtained from the surface winds and the PBL model, a least-squares optimization technique is used to find the best-fit, zero-mean surface pressure pattern that matches the pressure gradient field. If pressure observations are available, the average difference between them and the zero-mean field is the least-squares optimal estimate of what is effectively the integration constant that results from converting pressure gradients into a pressure field.

The premise of using pressure data for SAR wind Cal/Val is based on the following fact: Even without using ancillary data to set the absolute value of the pressure field, the bulk pressure gradient (BPG)

between any two points in the SAR-derived pressure field is the optimal estimate of that pressure difference derived from the SAR imagery. Hence pressure differences are more useful than point-by-point pressure comparisons assessing the quality of surface wind retrievals. Furthermore, the surface wind field is driven in large part by the pressure gradients, so wind vector errors and pressure difference errors are directly related.

The derived SLP patterns may be used as inputs to the PBL model to re-derive an "SLP-filtered" surface wind field. This product is a scene-wide estimate of the surface wind vectors that enforces consistency between the all of the wind vectors and the pressure fields. We have extensively documented this overall methodology and the high quality of our SLP fields and derived wind vectors using QuikSCAT and ASCAT scatterometer wind vector data in several papers (Patoux et al. 2003; 2008; 2011).

Our applications to TC conditions with SAR wind vectors have shown that both the directions and speed in the SLP-filtered winds can be significantly changed. In particular, the GMFs in high winds work best when the surface winds are across the radar beam and work poorly when the radar beam looks either up- or down-wind. The SLP-filtered winds "fill-in" the low wind holes near the TC core in these up- and down-wind regions. They can also fill in regions in the SAR WiSAR product that have been masked due to rainy conditions or for being out of range of the GMFs. Prior to the ITOP field campaign, we had only a handful of good SAR cases to study with near-in-time in situ data such as dropsondes and stepped-frequency microwave radiometer (SFMR) surface wind speeds. Examination of these cases has shown that the SLP-filtered wind speeds are a major improvement over the input wind speeds. A qualitative inspection of the wind directions suggests that they are more realistic than the input directions, which tend to have too little inflow in the inner core region. However, validation of wind directions is currently on-going using data from the ITOP experiment.

We now describe how a SAR-derived pressure field can be used to calibrate the surface winds. We pose the Cal/Val problem as an optimization problem in which we seek the minimum adjustment to the surface vector field that will minimize the difference between the SAR BPG and that derived from observations. A first-guess surface wind vector field from SAR is produced by WiSAR from which we calculate a first-guess surface pressure field. Given multiple surface pressure observations within this field, e.g. from dropsondes or aircraft-deployed buoys, we can calculate multiple, $M = N\left(N-1\right)/2$, BPGs within the image. The cost function to be minimized is the RMS difference between the SAR-derived BPGs and the observations along with constraints on the corrections to the wind field so that the optimization procedure does not impose unreasonable wind vector corrections. Assuming *M* BPG observations and *K* total surface wind vectors, the cost function is:

$$J = \sum_{n=1}^{M}\left(\Delta P_n^S - \Delta P_n^O\right)^2 + w_1\sum_{n=1}^{L}\left(S_n^{SAR} - S_n^{SFMR}\right)^2 + w_2\sum_{n=1}^{K}\left|\mathbf{u}_n - \mathbf{u}_n^0\right|^2 + \qquad (1)$$

The first term represents the RMS difference between the SAR and observed BPGs. The second term minimizes the difference between the SAR and SFMR surface wind speeds. The third term measures the RMS vector magnitude of the corrections to the original surface wind field and acts as a smoothness constraint – it penalizes large, localized wind vector modifications.

Each optimization step adjusts the surface wind vectors and recalculates the surface pressure field and the BPGs. The optimization treats the *U* and *V* components of the SAR winds separately since their error characteristics are approximately independent and Gaussian (Freilich, 1997). The computation

cost is nontrivial because each step in the optimization requires a new nonlinear surface pressure field in order to evaluate the cost function.

It should be emphasized that since surface pressure fields are integral properties of the surface vector wind fields, wind adjustments must occur over a broad spatial region rather than just locally near the pressure data. Thus, even though we use point wise pressure data, they imply wind corrections at a large number of wind vector cells.

WORK COMPLETED

Completed tasks: (1) Working version of SLP retrieval code, including necessary PBL model developments, that is compatible with GD, NURC and WiSAR file formats (as well as for ultra-high resolution QuickSCAT scatterometer files) has been developed, extensively tested and installed at CSTARS. (2) SLP code has been installed at NURC and we have been experimenting with Horstmann to determine if it can (or should) be included as an integrated part of the NURC SAR wind retrieval system. (3) Test version of the Cal/Val optimization scheme has been developed in FORTRAN. At present it uses an older version of the PBL model and SLP retrieval scheme. Only preliminary tests have been performed. (4) Data from the ITOP field program have been processed through the system and wind and SLP fields have been placed on the ITOP data catalog.

RESULTS

Much of the research involved a collection of historical Canadian RadarSAT-1 SAR images from the Hurricane Watch Program provided through an announcement of opportunity by the Canadian Space Agency, NOAA, NASA and CSTARS. From this collection, we examined a number of typhoons and hurricanes. The methodologies were developed and improved using these data prior to the ITOP field program. For the purposes of this report, we focus on the ITOP data from three images of Western pacific typhoons that span the range from a weak Cat-1 typhoon to a Cat-5 super-typhoon and from excellent in situ data to no in situ data.

Typhoon Malakas, 22 Sep, 2010, 20:30 UTC

At the time this image was acquired, Malakas had just reached typhoon strength. It also has the best in situ data coverage of any of the images. The C-130 aircraft was within the SAR scene at the time of acquisition for very complete storm survey between 20:00 to 01:00 (23^{rd}) UTC that included 31 drop sondes and SFMR winds. Because the storm was a weak Cat-1, the wind speed range was within reach of the standard GMF, CMOD5N. The image was acquired in HH polarization, so we had to apply the Thompson and Beal (2000) polarization correction using the parameter $\alpha = 0.8$. The storm center was in the low incidence angle region of the image, so saturation was an issue.

The C-130 data were mapped to the SAR image using a two-step process. First, we used the HRD flight-level storm center estimates to find the best-estimate eye location for the complete C-130 storm survey. Similarly we calculated the eye location for each time along the drop sondes' descents. From these, we calculated the distance and azimuth from the storm center for each individual SFMR or sonde measurement. An initial estimate of the storm center at the SAR overpass time was interpolated from the HRD best track. Adjusted latitudes and longitudes relative to this center were calculated from the instantaneous distances and azimuths. The HRD center estimate at the overpass time can differ from the center directly estimated from the SAR image due to errors in the flight level estimates, tilt in

the storm with height and the possibility of multiple circulation centers. So, a final constant translation to be applied to all of the adjusted data locations is obtained from the difference between the SAR and HRD centers. The C-130 flight track normalized to the SAR overpass time is shown in Figure 1.

Figure 2a shows the input wind field using the merged GD/NURC wind directions and the CMOD5N GMF. This is a descending pass and the low incident angles are along the right edge of the image. The winds were retrieved on 1 km pixels. The white vectors are spaced 30 km apart and have uniform length. The superposed black vectors are 10 m wind directions from the C-130 drop sondes. The sonde surface wind speeds are plotted as white-outlined boxes with the same colormap as the SAR wind speeds; they should fade into the background if the speeds agree. Figure 2c shows the derived SLP pattern normalized using the drop sonde splash pressures, which are shown a color shaded white-outlined boxes. The SLP-filtered winds are shown in Figure 2b. Note the significant changes in both wind speed and direction between the SLP-filtered winds and the raw CMOD5N input winds.

The SAR wind speeds are compared with the SFMR surface wind speed estimate in Figure 3a. SFMR surface wind speeds are calibrated to 1-min average winds; SAR wind speeds represent 10-min averages. The SAR winds are multiplied by 1.2 (Harper et al. 2010) to compensate for the differences in GMF calibration. Both the raw and SLP-filtered speeds compare well, but the SLP-filtered winds track SFMR better. A first check on the SAR-derived SLP is shown in Figure 3b. The C-130 flight-level data include an estimate of the surface pressure below the aircraft. The SAR SLP underneath the C-130 tracks the C-130 surface pressures quite well.

The best test of the methodology is shown in Figure 4a. The SAR SLP pattern is normalized to the drop sondes and the relatively small scatter shows that the shape of the pressure pattern is good. A better test is shown in Figure 4b, which compares the pressure differences between all pairs of sonde surface pressures with the corresponding SAR SLP pressure differences. If the shape of the retrieved pressure pattern is accurate, the slope of the best fit line should be unity. The in situ data confirm that the SAR-derived SLP pattern agrees well with the drop sonde data.

Overall, the comparison between the SAR SLP field and the SLP-filtered winds with the C-130 data shows that the methodology has worked very well in this case. There are evident issues with the wind retrievals in the low incidence angles (northeast side of the storm). In these cases the CMOD5N model could not match the backscatter and selected the closest match to the backscatter for the given viewing geometry. Because the SLP-filtering acts as a scene-wide retrieval, it finds that slightly different wind directions are a better overall fit to the inputs. The GMF in high winds and low incidence angles is very sensitive to the wind direction. If the SLP method is viable, we can use the SLP-derived wind directions to improve the CMOD5N wind retrievals. We use the SLP-filtered directions as inputs to CMOD5N and produce a new wind field iteratively. The results are shown in Figure 5. Figure 5a shows the raw input winds. The dark blue patch to the northeast of the storm center is the region of no CMOD5N retrieval. Figure 5b shows the result of a single iteration using SLP-filtered directions and Figure 5c shows the result of a second iteration. Note that the region of no solution shrinks after each iteration.

Typhoon Megi 15 October, 2010 21:00 UTC

Typhoon Megi was a very small, very strong typhoon that propagated rapidly across the Pacific. The compact size presents a major challenge to the PBL model used in the SLP retrieval, and the results show the further research is needed to improve its performance for storms of this type. At the time the

image was acquired, the C-130 aircraft was dispatched from Guam to deploy a string of buoys across the predicted path of the storm. It made a mini survey of the storm on its return flight about six hours after the satellite overpass. So, there is much less in situ data and that data have a large difference with the overpass. However, according to the JMA best track, the storm strength did not increase significantly during this time. The aircraft data were adjusted to the SAR image time as described above; the adjusted track is shown in Figure 6.

The input and SLP-filtered surface winds are shown in Figure 7ab and the SLP field is shown in Figure 7c. The small size of Megi relative to Malakas is evident. The SFMR wind speeds are plotted on Figure 7ab using the same colormap as the SAR winds, and they evidently agree better with the SLP-filtered winds than with the raw CMOD5N winds. However, the sonde surface wind and splash pressures have larger disagreement with the SAR winds and SLP.

The SFMR surface winds and C-130 flight-level surface pressure estimates are compared to the raw and SLP-filtered SAR winds in Figure 8a. The agreement is best for the SLP-filtered winds on the first SW-to-NE transect of the eye and on the final eye-to-SE transect. The SAR/C-130 surface pressure comparison in Figure 8b suggests that the PBL model in the pressure retrieval system is having difficulty capturing the very strong pressure gradients in this very compact storm. Some of this error might be associated with a low bias in the raw input winds. The scatter plots of pressure differences between the sonde splash pressures and the SAR SLP are consistent with too weak pressure gradients in this case (Figure 9). Improving the model's performance in compact storms is a focus of the research during the follow-on grant.

Typhoon Megi 17 October, 2010 21:41 UTC

This image captured Megi near the time that it reached super-typhoon status and just before it made landfall on Luzon. JMA estimated a central pressure of 885 mb and peak winds of 64 m/s. A C-130 drop sonde from about 9 hours earlier measured a peak near-surface wind speed of 85 m/s. This flight was the closest in time to the satellite overpass, but the JMA best track showed that the storm was continuing to deepen by at least 12 mb. Hence, for this case we do not have reliable in situ data for comparison even as it represents the most severe possible challenge to wind and pressure retrieval due to its small diameter and extreme strength.

A major issue with the high wind behavior of C-band GMFs in high winds is they become multi-valued, with high and low estimates of wind speed. Usually we use the lower wind speed ambiguity. In this case however, it was not possible to generate a reasonably deep SLP field from this image. So, a small number (fewer than 200 pixels) of high wind ambiguities replaced the lower ambiguities in the inner core region. The criteria were that the radius from the eye had to be less than 35 km and the high ambiguity could not be more than 60 m/s stronger than the low ambiguity.

The input winds, SLP-filtered winds and SLP are shown in Figure 10. The pressure field was normalized using the sonde splash pressures from the C-130 flight from 9 hours earlier without correction for further storm intensification. The most interesting feature of this case is the suggestion of a double eyewall in the SLP-filtered winds. Validating this structure is the focus of current research in the follow-on grant.

Partial Summary of Drop Sonde Surface Pressure Results

Figure 11 show a summary from four Atlantic hurricanes and two cases from ITOP (excluding Megi) of the drop sonde splash pressure differences and SAR-derived pressure differences. Overall the agreement is quite good, although further research should reduce the scatter. Because the Megi results are inconsistent with these other cases further research is needed to improve the PBL model performance for the condition of small and intense storms.

Organized Surface Stress Convergence Lines

This research did find strong, but preliminary, evidence a new level of organization in the near-surface boundary layer with characteristic wavelengths of ~ 10 km. Previous research had documented that low aspect ratio (wavelength/PBL depth) PBL-spanning roll vortices are a very common feature of hurricane and typhoon boundary layers. Foster (2005) presented a theoretical explanation why they ought to be the expected state of the tropical cyclone boundary layer. These rolls form at small angles to the mean PBL wind and have typical wavelengths of about 2.5 to 4 times the PBL depth, or nominally 1500 to 2500 m. Hence, their effects should not be resolved in these 1-km pixel wind speed images. (Note however that their imprint can be resolved in the raw 10 to 25 m SAR pixels. This imprint is used to make the first guess at wind directions in the wind speed retrieval process.) Although the strongest direct effect of the rolls is a periodic enhancement and reduction of the mean azimuthal winds in the radial direction, there is an associated overturning circulation that induces alternating bands of convergence and divergence, with the same 1.5 to 2.5 km spacing as the rolls, in the surface wind field.

One major benefit of the scene-wide, SLP-filtered wind retrievals is that it is possible to make sensible calculations of wind vector gradients. Figure 12 shows surface wind convergence fields calculated from SAR images of six hurricanes and typhoons. They all show a high degree of organization on multi-km (~10 km) scales. These patterns are roughly aligned along the surface wind direction and hence bear a lot of similarity to the PBL rolls seen in observations (Wurman and Winslow Morrison et al., 2005; Lorsolo et al. 2008; Zhang et al. 2008; Ellis and Businger, 2010) and theoretically derived in Foster (2005). What remains to be explained is their very large aspect ratio, which is on the order of 5 to 10. Even though the observations in Morrison et al. (2005) were dominated by the low aspect ratio roll modes, their observations documented that a small fraction of their roll observations were from high aspect ratio rolls. Possible explanations are coupling with tropospheric gravity waves, nonlinear roll-roll interactions and coupling to convection. Their dynamical role is also unknown. They may contribute to nonlocal (i.e. non-gradient) fluxes of enthalpy and momentum across the PBL or they might precondition the PBL and lower troposphere for future convection bands.

We recently became aware (Prof. Gregory Tripoli, pers. comm.) of some numerical modeling studies that find 10 km scale roll vortices throughout their boundary layer outside of the radius of maximum wind. Near-surface convergence plots from their numerical model are a good match to the SAR observations. They attribute these large aspect ratio rolls to a mechanism similar to that described in Foster (2005).

It should be noted that the theory in Foster (2005) does indeed predict that nonlinearly stable, large aspect ratio rolls (~10) are possible. Figure 13 reproduces Figures 4 and 7 from Foster (2005). The interpretation of Figure 13a is that a wide range of wavenumbers with a range of orientation angles are unstable (positive growth rate). All of these unstable modes are roll vortices that vary primarily in

wavelength and orientation relative to the mean wind. The fastest growing modes agree with the low aspect ratio rolls that have been documented in the observational studies. However, large aspect ratio rolls (corresponding to wavenumbers, α, near 0.25 are also linearly unstable, although more slowly growing than the low aspect ratio roll modes. Furthermore, Figure 13b shows that all linearly unstable modes are nonlinearly stable – that is, the exponential growth is checked by self-modification and modifications of the mean flow in a manner that the rolls and mean flow equilibrate into a new mean state with finite non-local fluxes of heat and momentum. So, large aspect ratio rolls that could match the structures seen in the SAR in the convergence fields are consistent with theory of Foster (2005).

Because the large aspect ratio roll modes grow more slowly than the basic roll modes, all things being equal, they would not at first be expected to survive the "competition" for extracting mean flow energy. However, Mourad and Brown (1990) demonstrated that nonlinear roll-roll interactions are a viable mechanism for coupling energy from the initially faster growing low aspect ratio rolls into the large aspect ratio rolls. The coupled system finds a new equilibrium in which the high aspect ratio rolls coexist with the low aspect ratio rolls. This mechanism was used to explain the observations of cold air outbreaks off the pack ice in which both large and small aspect ratio rolls were found to coexist. A similar mechanism may be in play in the hurricane boundary layer. This is an exciting avenue for new research.

These features are an unexpected result of this research and future research efforts will focus on developing a dynamical explanation for their formation and maintenance and on uncovering what role they play in typhoon physics.

IMPACT/APPLICATIONS

The strong correlation between the derived SLP and the observations suggests that the Cal/Val optimization strategy has strong potential. Those results should have a significant positive effect on future SAR wind retrievals in TC conditions. This will be pursued in future research.

PUBLICATIONS

We are currently writing papers describing the methodology and results described in this report.

Presentations:

Foster, RC, J Patoux and RA Brown, "Applications of OVW-Derived Surface Pressures in Tropical Cyclones", 2010 International Ocean Vector Winds Meeting, Barcelona, Spain, 18-20 May, 2010.

Foster, RC : "An Innovative Method for Validating Surface Winds Derived from SAR Imagery for Tropical Cyclones" RADARSAT Hurricane Applications Workshop, Canadian Space Agency, John H. Chapman Space Centre, Saint-Hubert, Quebec, 5 Oct. 2010

Foster, RC and J Patoux: "Using Surface Pressure to Improve SAR High Wind Retrieval in Tropical Cyclones", PO25J-04, Ocean Sciences Meeting, Portland, OR, 21-25 Feb, 2010.

Foster, RC and J Patoux: "Diagnosing tropical cyclone surface wind fields from SAR", 17th Conference on Air-Sea Interaction, Amer. Meteor. Soc., Annapolis, MD, 27-30 Sep, 2010.

Foster, RC, J Patoux, C Wackerman, J Horstmann, S Falchetti, R Romeiser, M Caruso, H Graber: "Sea-level Pressure and Surface Wind Retrievals Derived From Satellite Synthetic Aperture Radar Images of Tropical Cyclones During ITOP", Impact of Typhoons in the Pacific (ITOP) Meeting, Santa Fe, New Mexico, 17-20 May 2011

REFERENCES

Ellis, Ryan S Businger 2010: Helical circulations in the typhoon boundary layer. *J. of Geophys Res* **115**, D06205, doi:10.1029/2009JD011819

Foster RC 1997: Structure and energetic of optimal Ekman layer perturbations, *J Fluid Mech*., **333**, 97-123.

Foster, R. C., 2005: Why rolls are prevalent in the hurricane boundary layer. *J. Atmos. Sci*., **62**:2647–2661.

Foster RC 2009: Boundary-layer similarity under an axi-symmetric, gradient wind vortex. *Bound.-Lay Meteorol*. **131** 321-344.

Freilich, MS 2001: Validation of Vector Magnitude Datasets: Effects of Random Component Errors, *J Atmos. Ocean Tech*, **14**, 695-703.

Harper, B. A., J. D. Kepert, and J. D. Ginger, 2010: Guidelines for Converting between Various Wind Averaging Periods in Tropical Cyclone Conditions. World Meteorological Organization, TD-1555, 64 pp.

Lorsolo S, J L. Schroeder, P Dodge, F Marks Jr. 2008: An Observational Study of Hurricane Boundary Layer Small-Scale Coherent Structures, *Mon Wea Rev*. **136**, 2871-2893

Morrison, I., S. Businger, F. Marks, P. Dodge, and J. A. Businger, 2005: An observational case for the prevalence of roll vortices in the hurricane boundary layer. *J. Atmos. Sci*., **62**:2662–2673.

Mourad PD and RA Brown 1990: Multiscale large eddy states in weakly stratified planetary boundary layers, J. Atmos. Sci., 47, 4, 414-438

Patoux J, RC Foster and RA Brown, 2003: Global pressure fields from scatterometer winds, *J Appl Meteorol*., **42** 813-826.

Patoux, J Foster RC and RA Brown 2008: An evaluation of scatterometer-derived ocean surface pressure fields, *J Appl. Meteor. Clim*. **47**, 835-853.

Patoux, J, RC Foster and RA Brown, 2011: Cross-validation of scatterometer measurements via sea-level pressure retrieval, submitted to *J Geo Phys. Res*.

Thompson, DR and RC Beal 2000: Mapping high-resolution wind fields using synthetic aperture radar, Johns Hopkins Tech. Dig. 21, 58-67.

Wurman J and Winslow 1998: Intense Sub-Kilometer-Scale Boundary Layer Rolls Observed in Hurricane Fran, Science, 280 555-557.

Zhang, J. A., K. B. Katsaros, P. G. Black, S. Lehner, J. R. French, and W. M. Drennan, 2008: Effects of roll vortices on turbulent fluxes in the hurricane boundary layer. *Bound-Layer Meteor*. **128**, 173-189.

FIGURES

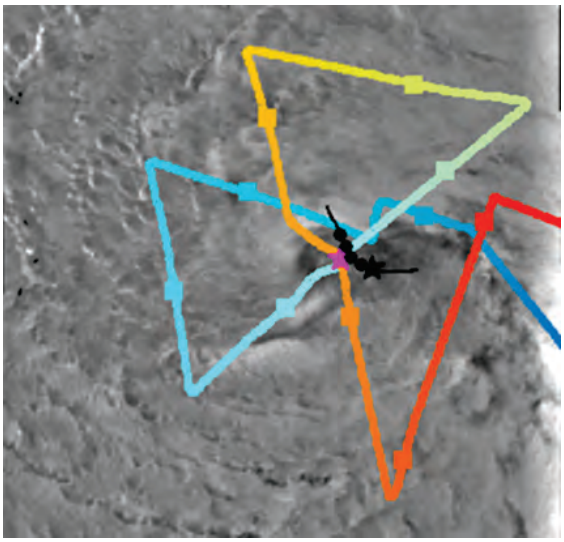

Figure 1: C-130 storm survey of typhoon Malakas, 22 Sep, 2010, 20:00 to 01:00 (12th) UTC superposed on the SAR image acquired 22 Sep, 2010, 20:30 UTC. The track has been adjusted to the overpass time as described in the text. Color shading shows increasing time (blue to red), squares are 30 m. apart. HRD/Willoughby storm center track is shown in black; dots are 60 min. apart. SAR storm center is magenta star; HRD center at 20:30 is black star.

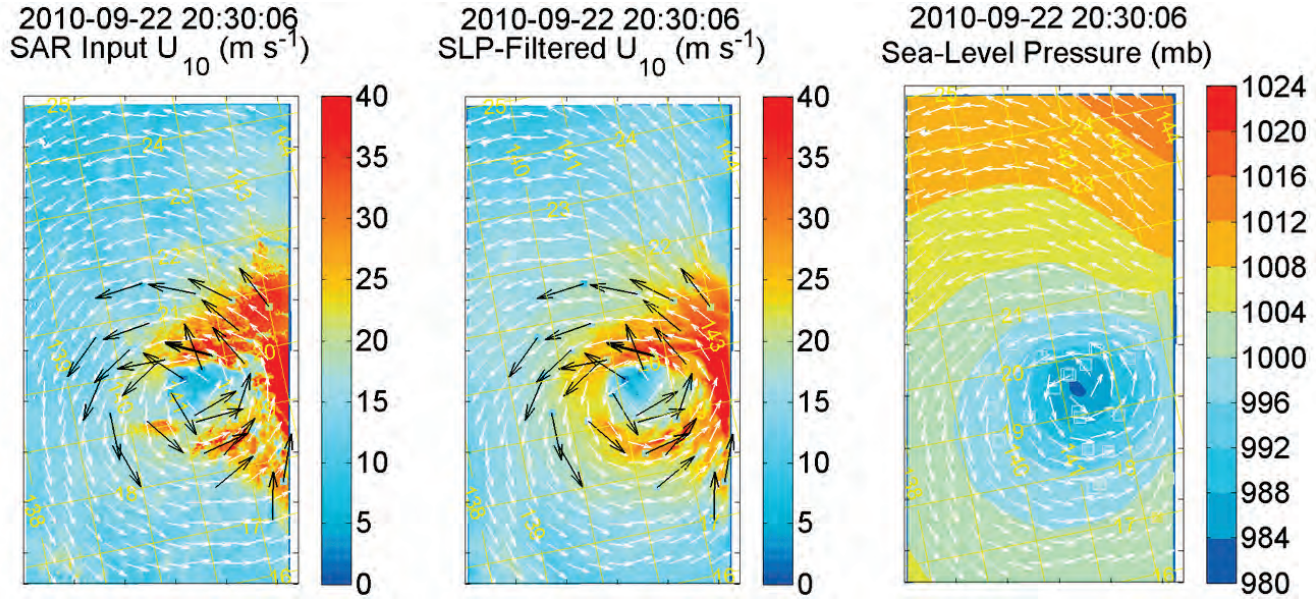

Figure 2: Malakas 22 Sep 2010, 20:30 UTC. (a) Raw input winds derived from merged GD/NURC wind directions and CMOD5N. (b) SLP-filtered surface winds. (c) SAR-derived sea-level pressure (SLP). The wind vectors have uniform length and show the SAR directions at 30 km spacing. The black vectors show the sonde 10 m directions. In (a) and (b) the sonde 10 m wind speeds are shown in white outlined squares. In (c) the boxes are the sonde splash pressures.

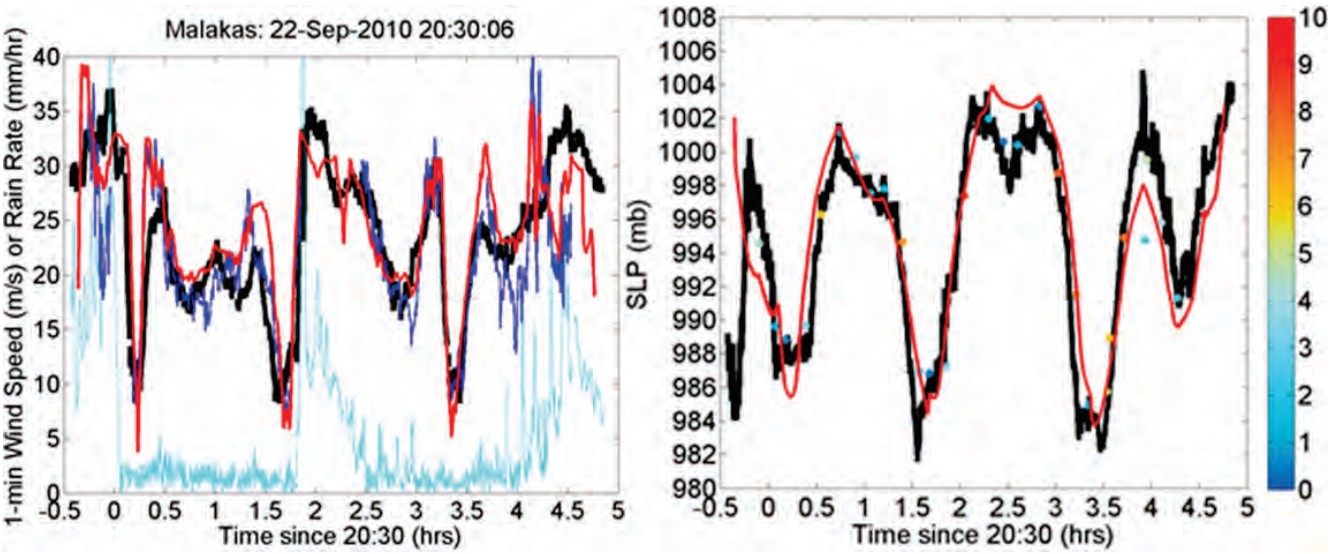

Figure 3: Malakas, 22 Sep 2010 20:30 UTC. (a) Comparison of SAR surface wind speeds with C-130 SFMR wind speeds (black). The raw SAR wind speeds are in blue and the SLP-filtered wind speeds are in red. The SFMR rain rate is in cyan. The SAR winds have been multiplied by 1.2 to correct for the different mean wind scaling (~10 min for SAR and ~1-min for SFMR). (b) Estimate of surface pressure from C-130 flight level data (black). SAR SLP in red. Closest sonde splash pressures to C-130 sub-aircraft point are plotted as dots color coded as distance in km of the splash point from the aircraft.

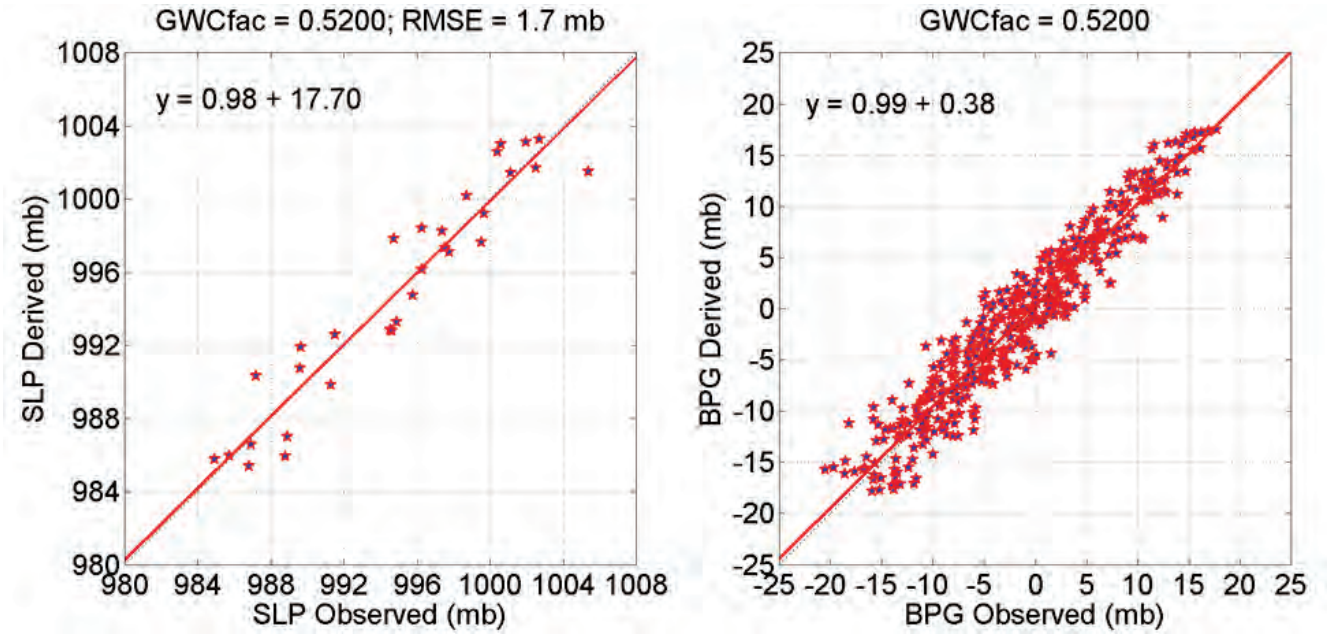

Figure 4: Malakas 22 Sep 2010, 20:30 UTC. (a) Comparison of sonde splash pressure with SAR-derived pressure. (b) Comparison of bulk surface pressure differences between all pairs of drop sondes and the SAR SLP.

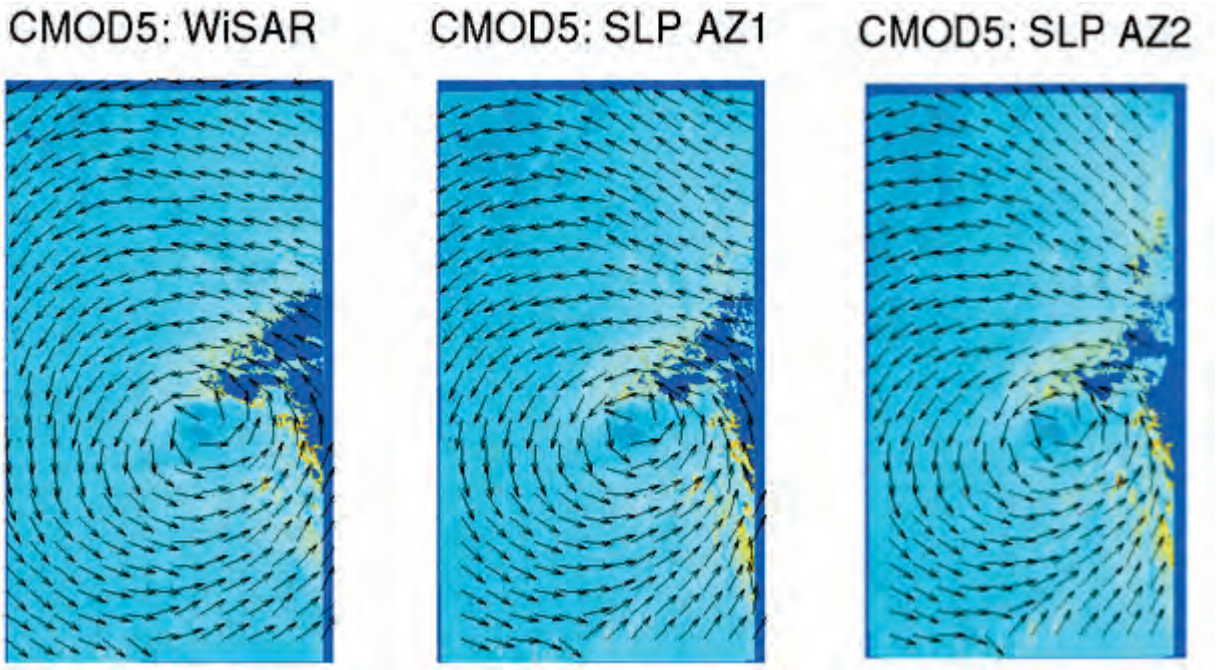

Figure 5: Malakas 22 Sep 2010, 20:30 UTC. Effect of using SLP-filtered wind directions to improve CMOD5N retrievals in high wind and low incidence angle conditions. (a) raw speeds using GD/NURC directions. (b) Retrieved speeds using SLP-filtered wind directions (1 iteration). (c) Retrieved speeds using SLP-filtered wind directions (2 iterations). The region of no solution is the dark blue. Note how it shrinks when SLP-filtered directions are used.

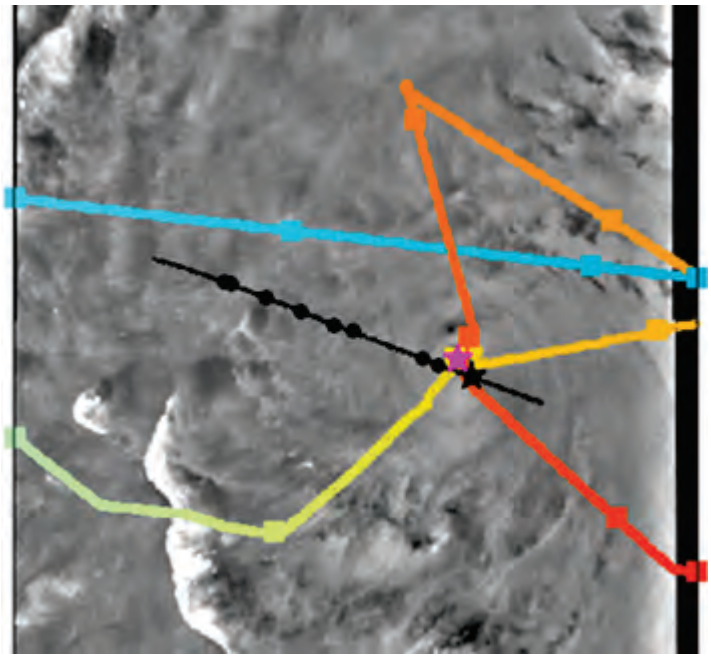

Figure 6: Typhoon Megi 15 October 2010, 21:00 UTC. Adjusted C-130 flight track. Symbols as in Figure 1.

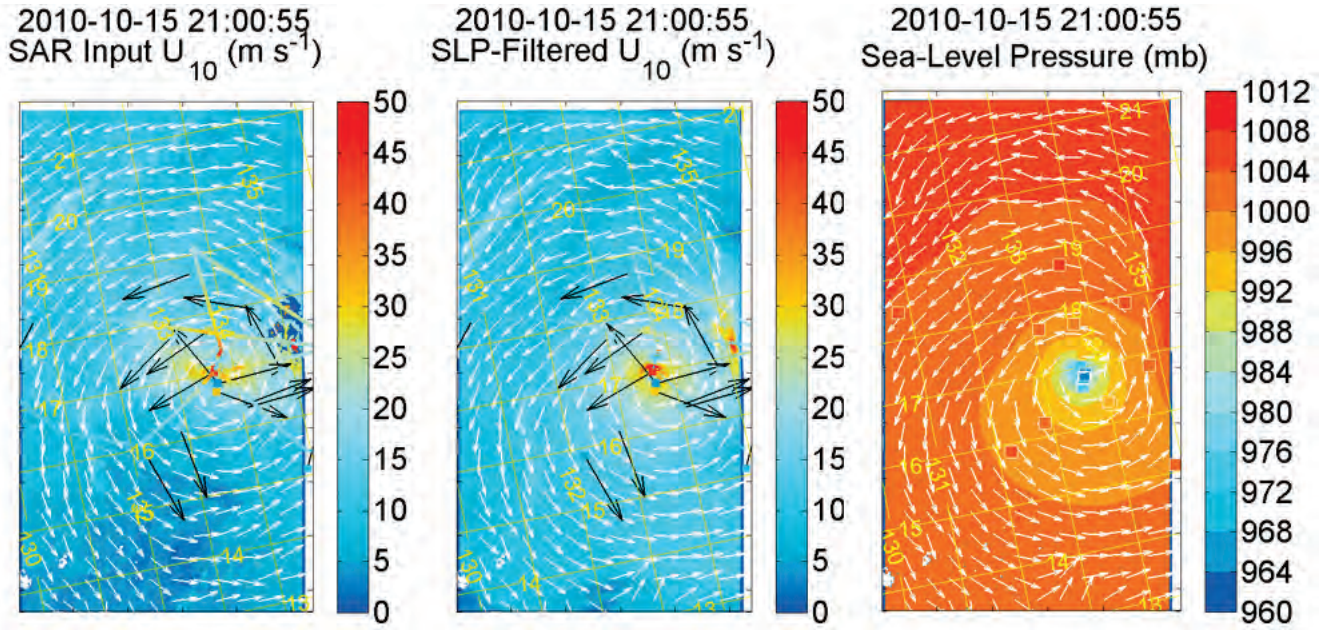

Figure 7: Typhoon Megi, 15 Oct 2010, 21:00 UTC. As in Figure 2. Also plotted is the SFMR wind speed using the same color map as the SAR wind speed.

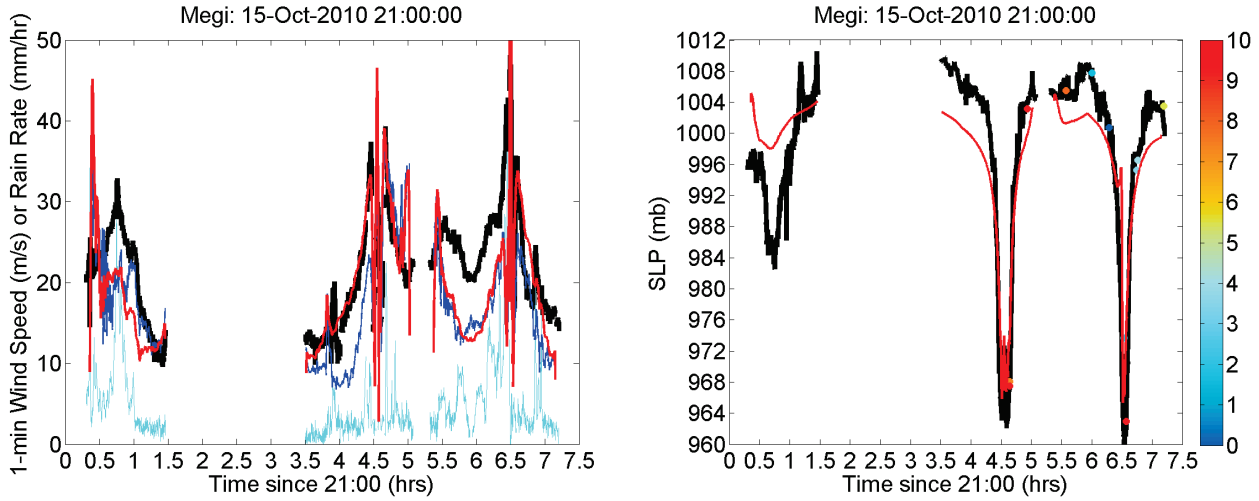

Figure 8: Typhoon Megi, 15 Oct 2010 21:00 UTC. As in Figure 3.

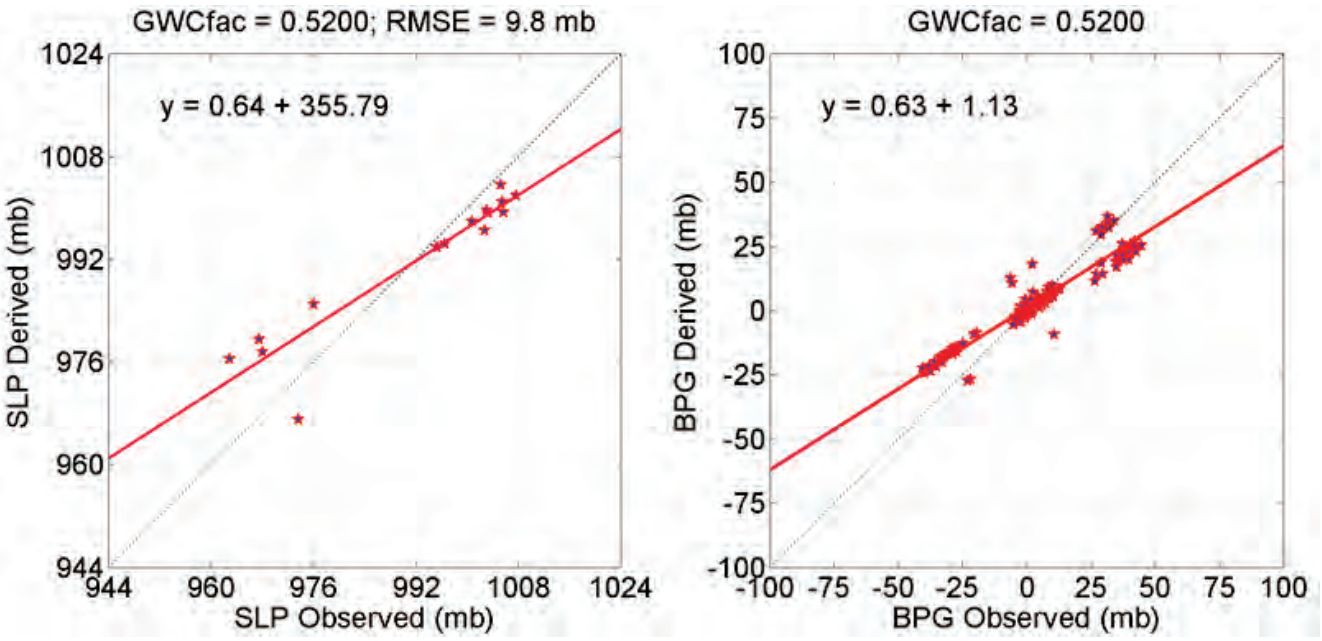

Figure 9: Typhoon Megi, 15 Oct 2010 21:00 UTC. As in Figure 4.

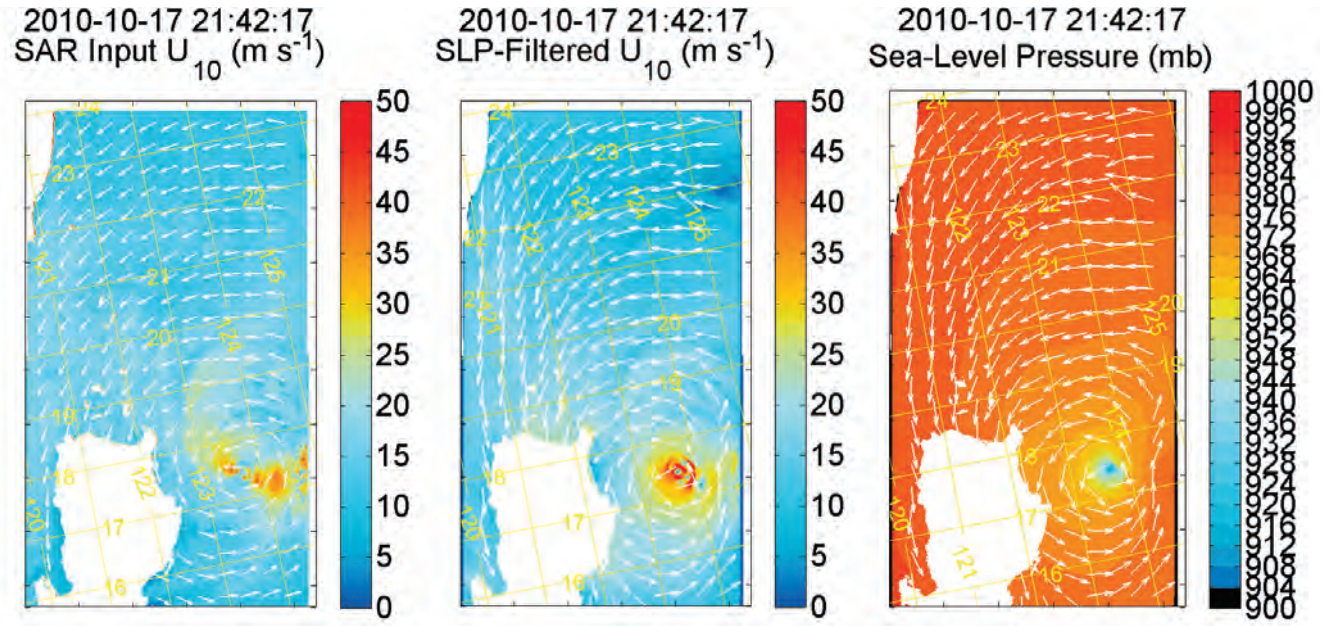

Figure 10: Supertyphoon Megi, 17 October 21:41 UTC. As in Figure 2.

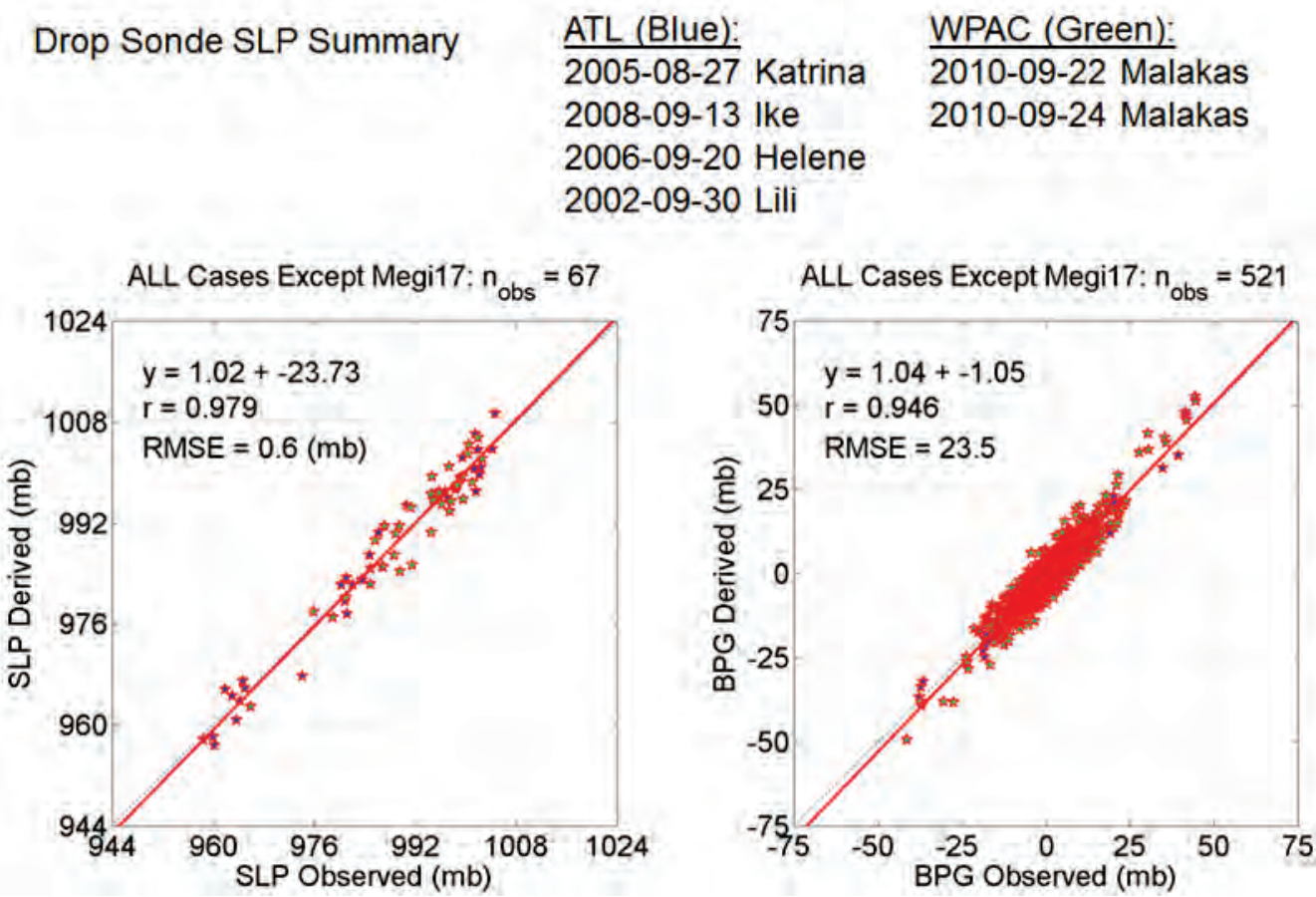

Figure 11: As in Figure 4. Summary of drop sonde comparisons for four Atlantic hurricanes and two ITOP typhoons.

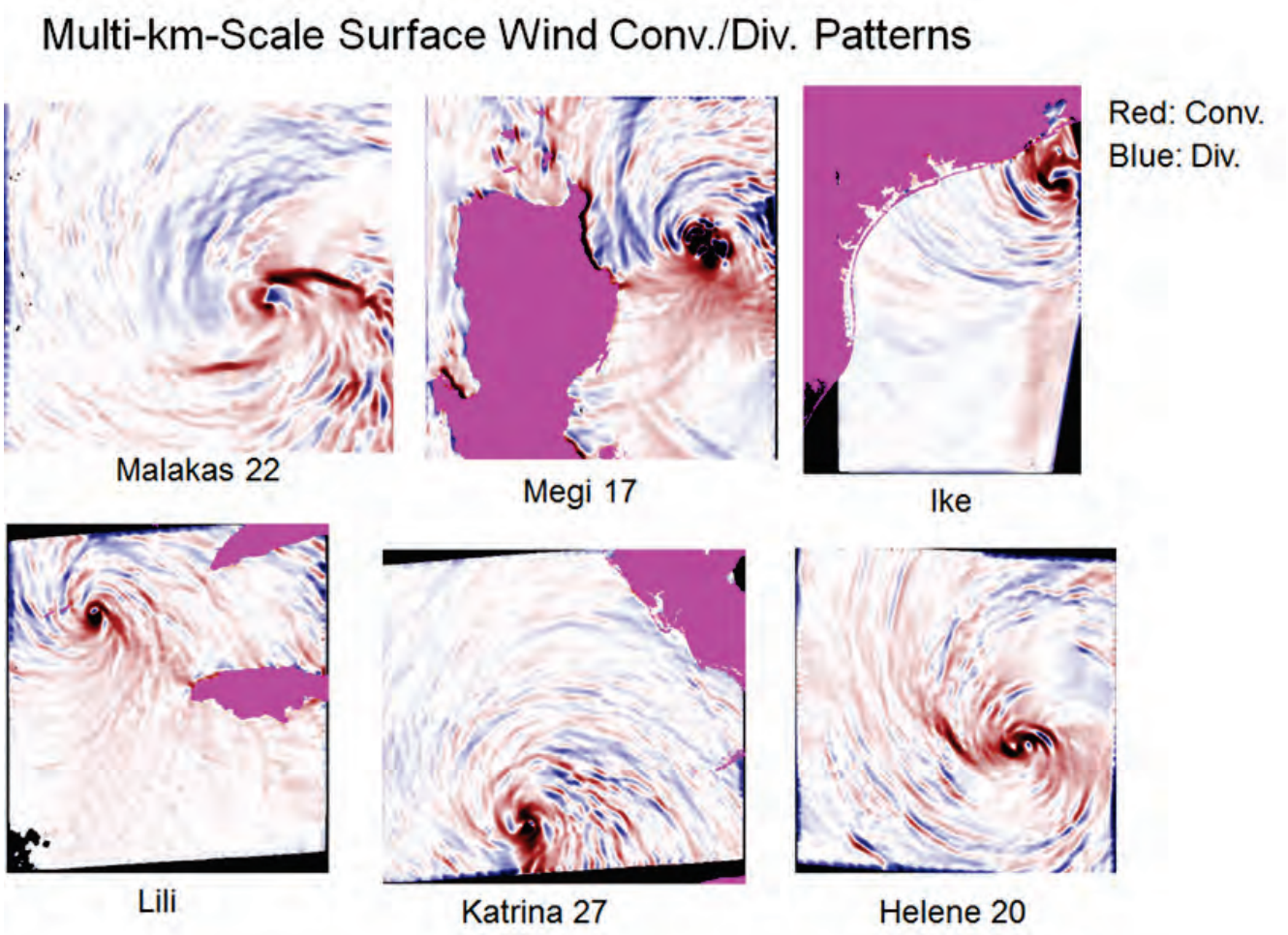

Figure 12: Surface wind convergence fields calculated from the SLP-filtered winds for six hurricanes and typhoons. The spacing between the bands is about 10 km.

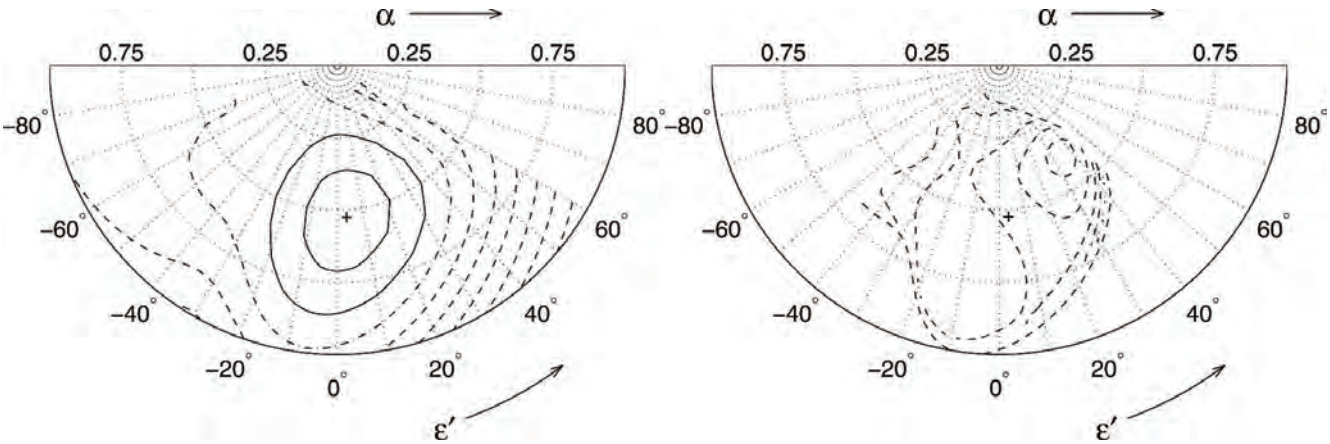

Figure 13: (a) Figure 4 and (b) Figure 7 from Foster (2005). The original captions are: FIG. 4. Linear instability growth rate a_0 as a function of angle from azimuthal wind $\varepsilon' = \varepsilon - 90°$ and wavenumber α for r = 40km and ΔT = - 5 K. Solid lines denote positive growth rates, dash–dotted lines denote zero growth, and dashed lines denote negative growth rates. Contour interval is 0.005 (nondimensional). The equivalent plot for neutral stratification is very similar with overall reduced growth rates and the peak shifted toward larger ε'. FIG. 7. First Landau coefficient a_1 corresponding to the conditions in Fig. 4 for $a_0 > 0$. The $a_0 = 0$ contour is shown as dash–dot. Contour interval is 0.0005 (nondimensional).

REPORT DOCUMENTATION PAGE

Form Approved
OMB No. 0704-0188

PLEASE DO NOT RETURN YOUR FORM TO THE ABOVE ADDRESS.

1. REPORT DATE *(DD-MM-YYYY)*	2. REPORT TYPE	3. DATES COVERED *(From - To)*
19-03-2012	Final Report	01 August 2008 to 31 December 2011

4. TITLE AND SUBTITLE

Final Report: Using Surface Pressure to Improve Tropical Cyclone / Surface Wind Retrievals from SAR

5a. CONTRACT NUMBER

5b. GRANT NUMBER

N00014-08-1-1640

5c. PROGRAM ELEMENT NUMBER

6. AUTHOR(S)

Ralph Foster
Jerome Patoux

5d. PROJECT NUMBER

5e. TASK NUMBER

5f. WORK UNIT NUMBER

7. PERFORMING ORGANIZATION NAME(S) AND ADDRESS(ES)

Applied Physics Laboratory - University of Washington
1013 NE 40th Street
Seattle, WA 98105-6698

8. PERFORMING ORGANIZATION REPORT NUMBER

9. SPONSORING/MONITORING AGENCY NAME(S) AND ADDRESS(ES)

Office of Naval Research (ONR 322)
875 North Randolph Street
Arlington, VA 22203-1995

10. SPONSOR/MONITOR'S ACRONYM(S)

ONR

11. SPONSOR/MONITOR'S REPORT NUMBER(S)

12. DISTRIBUTION/AVAILABILITY STATEMENT

Distribution Statement A: Approved for public release: distribution is unlimited

13. SUPPLEMENTARY NOTES

None

14. ABSTRACT

Synthetic aperture radar (SAR) images of the sea surface underneath tropical cyclones have the potential to provide air-sea interaction data at km-scale resolution. However, many challenges remain in extracting such data in these extreme environments. This research focused on the problem of extracting surface vector wind and sea-level pressure fields from the SAR images. The geophysical model functions (GMFs) that describe the radar backscatter are currently poorly characterized for the very high winds and sea states in tropical cyclones. Calibration and validation of GMFs is severely inhibited by the lack of accurate in situ surface wind data. We demonstrate that surface pressure data provides a more useful method for validating and improving surface vector wind retrievals and that scene-wide wind vector retrievals that employ our technique are superior to the standard pixel-by-pixel methodologies that are currently standard practice. Aircraft and in situ data from the Impact of Typhoons on the Pacific (ITOP) 2010 field program were used to develop and demonstrate the methodology.

15. SUBJECT TERMS

tropical cyclones, hurricanes, typhoons, synthetic aperture radar, sea-level pressure, satellite ocean vector winds, ITOP, boundary layer

16. SECURITY CLASSIFICATION OF:			17. LIMITATION OF ABSTRACT	18. NUMBER OF PAGES	19a. NAME OF RESPONSIBLE PERSON
a. REPORT	b. ABSTRACT	c. THIS PAGE			Ralph Foster
U	U	U	UU	17	19b. TELEPHONE NUMBER *(Include area code)* 206-685-5201

Reset

Standard Form 298 (Rev. 8/98)
Prescribed by ANSI Std. Z39.18